Study on the mechanism of burr formation in ultrasonic vibration-assisted honing 9Cr18MoV valve sleeve

Peng Wang[1] · Chang-Yong Yang[1] · Ying-Ying Yuan[1] · Yu-Can Fu[2] · Wen-Feng Ding[1] · Jiu-Hua Xu[1] · Yong Chen[3]

Abstract The precision, lifespan, and stability of the electro-hydraulic servo valve sleeve are significantly impacted by the edge burrs that are easily created when honing the valve sleeve. The existing deburring process mainly rely on manual operation with high cost and low efficiency. This paper focuses on reducing the burr size during the machining process. In this paper, a single-scratch test with a finite element simulation model is conducted to study the mechanism of burr generation. The tests were carried out under ultrasonic vibration and non-ultrasonic vibration conditions to explore the effect of ultrasonic vibration on burrs. Besides, a honing experiment is conducted to verify the conclusions. The results at various cutting parameters are analyzed, and the mechanism of burr generation is revealed. The stiffness lacking of the workpiece edge material is the main reason for the burr generation. The cutting depth shows a significant effect on burr size while the cutting speed does not. The inhibition mechanism of ultrasonic vibration on burrs is also revealed. The separation of the burr stress field under ultrasonic vibration and the higher bending hinge point is the reason for burr fracturing. The re-cutting effect of ultrasonic vibration reduces the burr growth rate. The results of the honing experiment verified these conclusions and obtained a combination of honing parameters to minimize the burr growth rate.

Keywords Honing · Ultrasonic vibration-assisted · Burr · Finite element simulation

1 Introduction

The electro-hydraulic servo systems are widely used in aviation, aerospace vehicles, ships, and rockets. The servo valve, which serves as the foundation of an electro-hydraulic servo system, is primarily utilized to accomplish precise control over displacement, speed, and torque [1, 2]. The core of a servo valve is a pair of spool valves made up of a spool and a valve sleeve [3]. The manufacture and assembly accuracy of the spool and valve sleeve, including shape accuracy, position accuracy, dimensional accuracy, and surface roughness, are the primary determinants of its performance.

However, due to the special structure of the valve sleeve, the edge of the intersecting bore in the valve sleeve is easy to produce burrs. The precision, lifespan, and stability of the valve sleeve are significantly influenced by these burrs [4] which are difficult to remove. In the existing deburring process, burrs with a small size can be removed using a metal brush, but it would also do harm to the surface quality of the valve sleeve bore. While removal of the burrs with a big size can only rely on manual operation. Generally, a deburring process is already arranged prior to the final finishing of the valve sleeve. Arranging another deburring process after the finishing is not only inefficient but also would increase the scrap rate. Therefore, it is necessary to inhibit the burr generation during the finishing process.

Usually, the burr is unavoidable and its shape, size, and forming process are various with the machining methods.

✉ Chang-Yong Yang
yangchy@nuaa.edu.cn

1 College of Mechanical and Electrical Engineering, Nanjing University of Aeronautics and Astronautics, Nanjing 210016, People's Republic of China

2 National Key Laboratory of Science and Technology on Helicopter Transmission, Nanjing University of Aeronautics and Astronautics, Nanjing 210016, People's Republic of China

3 Suzhou Xinneng Precision Machinery Co., Ltd, Suzhou 215000, Jiangsu, People's Republic of China

For example, the possible burr types in face milling are knife-type, wave-type, curl-type, edge breakout, and secondary burr [5, 6]. While those in face grinding are: positive burr, negative burr, and residual burr [7]. Among them, burrs with positive burr characteristics are the easiest to remove, so relevant research is usually aimed at generating such burrs and reducing their size.

In the orthogonal cutting process, the formation of burrs is related to cutting conditions, work material microstructure, and mechanical behavior. Increasing the uncut chip thickness will promote the formation of a negative burr while decreasing the uncut chip thickness will cause burr accumulation under continuous cutting. In the cutting process, significant local strain is the main cause of crack initiation, expansion, and eventually, fracture [8].

For machining methods with micro-removal characteristics, the most effective and commonly used method to study the burr formation process and influencing factors is finite element simulation (FES) analysis combined with a single-grain scratch test [9]. For example, in the grinding process, the factors that have a significant impact on the morphology and size of burrs are wheel granularity [10], uncut chip thickness [7, 10–12], negative rake angle of the abrasive grain [7, 12], grinding temperature [13], grinding force [12, 13], and the workpiece's chamfer size [11]. In the process of micro-milling, the burr size is determined by the relationship between the uncut chip thickness and the radius of the cutting edge [14, 15]. Pre-introduction of stress can inhibit the generation of burrs [16]. As for the honing process, the factors that affect the burr size include the penetration depth of the abrasive grain [17], the rake angle of the abrasive, and the number of times that the abrasive grain passes through the edge of the workpiece [18].

In recent years, researchers have paid more attention to how ultrasonic vibration (UV) influences the machining process at different machining methods. For the cutting process, Xu and Zhang [19] studied the advantages of applying UV on cutting, which showed high machining capabilities, including low cutting forces, long tool life, high surface integrity, and excellent cutting accuracy; Liang et al. [20] studied the material removal mechanism of high-frequency UV-assisted cutting. The defect-free surface can be obtained by making the cutting stroke in each vibration cycle less than 800 nm. Dynamic recrystallization can release the stress concentration. For the micro-milling process, Zhang et al. [21] proposed that applying high-frequency UV in the milling feed direction could reduce cutting temperature and cutting force, improve chip-breaking ability, and reduce burr formation; Chen et al. [22] conducted that the frequency of UV had a significant influence on the machining mechanism, e.g., suppression of burr formation and reduction of cutting forces and tool wear; Xu et al. [23] found that the longitudinal-torsional UV could reduce the burr length and

cutting force as well as release the concentrated stress. For micro-drilling, Zhu et al. [24] found that UV showed an effect of decreasing cutting force, inhibiting the burr formation, improving surface quality and the dimensional accuracy, and effectively hindering bit wear; Chang and Bone [25] developed an analytical burr height model for UV assisted drilling; Zai et al. [26] and Li et al. [27] studied the influence between the drilling parameters and burr size. The studies show that using a bigger amplitude, higher spindle speed, and lower feed speed can reduce the burr size. Much research indicates that the UV effect can reduce cutting force and burr size. Xiang et al. [28] studied the mechanism of the UV effect which was the intermittent cutting and high-frequency impact characteristics of ultrasonic vibration would reduce the fracture strength of the material, making it more prone to crack and fracture.

Among many of the finishing processes, honing is commonly used in finishing the valve sleeve, which can improve the surface quality and shape accuracy. Presently, there is already some research on ultrasonic-assisted honing (UAH). For example, Gao et al. [29] proposed that UAH could effectively decrease honing torque and improve honing efficiency. However, the burrs formation during UAH is a lack of research. This paper will focus on the burr's generation mechanism and the main influence factors on burr size during UAH process. The main work of this paper is as follows.

(i) The finite element simulation is used to study the law of burr evolution.
(ii) Single-grain scratch tests under UV and non-UV conditions are carried out to explore the influencing factors of burrs, and analyze the effect of UV on burrs with FES.
(iii) Honing tests under UV and non-UV conditions are carried out to verify the effect of UV on inhibiting the burr's generation during honing.

2 Method and materials

2.1 Motion analysis of UAH

To make the test and simulation more in line with the actual UAH situation, it is necessary to analyze the relative motion between the abrasive grain on the honing stone and the workpiece.

The relative motion of honing is compound, including rotation and reciprocation along the tool axis. Inside the honing tool, the axial feed of the expanding cone is converted into the radial feed of the honing stone through a cone surface, providing the normal force between the honing stone and the workpiece. The abrasive grains are fixed on the surface of the honing stone, cutting the workpiece
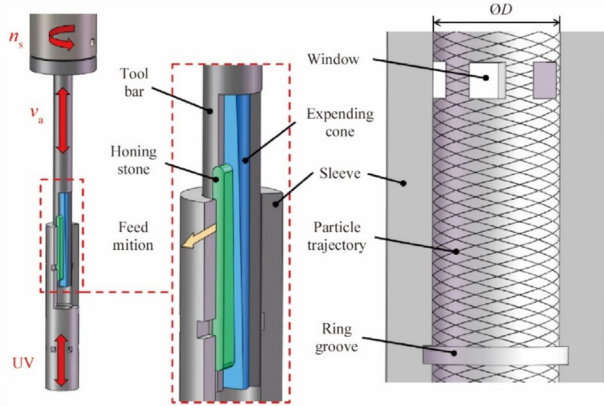
Fig. 1 Working principle of UAH

under relative motion and normal force, and forming cross-grained lines on the surface of the valve sleeve bore after honing, as shown in Fig. 1.

In the UAH process, due to the complex structure of the honing tool, the UV is usually applied on the workpiece along the axis direction of the honing tool. The relative motion trajectory between the honing stone and the workpiece can be described as

$$
\begin{cases}
x(t) = r\cos(\omega t), \\
y(t) = r\sin(\omega t), \\
z(t) = A\sin(2\pi ft) + v_a t,
\end{cases}
\tag{1}
$$

where ω is the angular velocity of the tool, r the radius of the honing tool, A the vibration amplitude, f the vibration frequency, v_a the axial velocity, and t is the time.

In this study, the frequency of the UV is set as 18 000 Hz, and the amplitude is set as 4 µm. Figure 2 shows the diagram of local trajectory of the honing stone under UV and non-UV conditions.

The abrasive grains are in a continuous cutting state during the honing process, and the cutting depth of any single grain on the honing stone is less than 5 µm, which is much smaller than the curvature radius of the valve sleeve bore. Therefore, in the simulation and experiment study, the movement of a single grain can be simplified as a continuous curve with a fixed cutting depth.

2.2 Single-grain scratch test setup

The most commonly used material of the sleeve is 9Cr18MoV, which belongs to high-carbon and high-chromium martensitic stainless steel. It has high hardness, high wear resistance, and high corrosion after quenching. The test surface of the workpiece is 10 mm × 3 mm in size, pretreated on the WAZA415X-NC ultra-precision forming surface grinder, which has a minimum feed of 0.1 µm. The roughness of the test surface was 0.4 µm and the flatness was 1 µm after pretreatment. The grain material is CBN, which is commonly used in metal cutting. It has high hardness, good wear resistance, high thermal stability, and good chemical stability. The diameter of grain used in the single-grain scratch test was 325−380 µm.

The single-grain scratch test was conducted at the DMG Ultrasonic 20 Linear ultrasonic assisted machining center, as shown in Fig. 3. The workpiece was fixed on the Kistler 9129AA dynamometer, measuring the cutting force during the test process. The CBN grain was brazed on the self-made UV tool, moving with the spindle of the machining center.
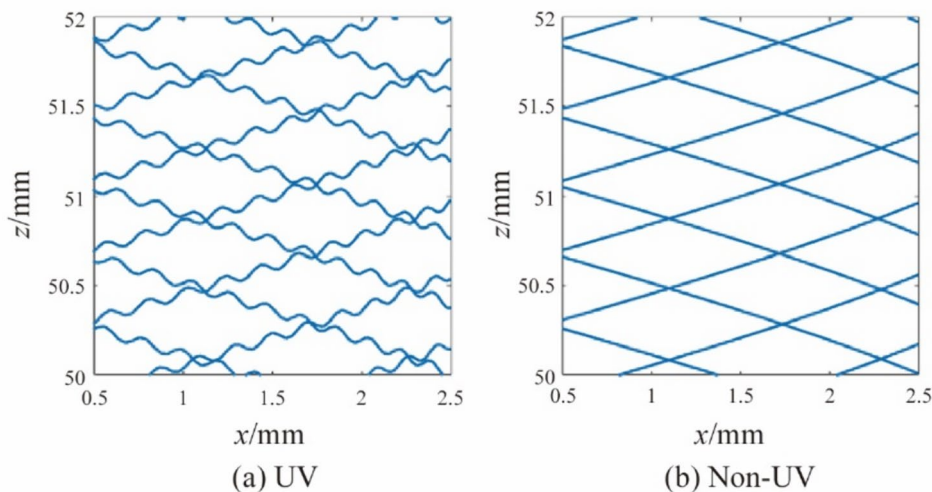

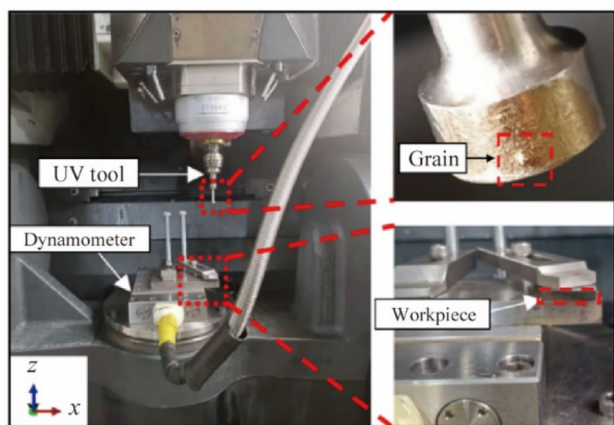**Fig. 2** Local trajectory of honing stone under UV and non-UV conditions
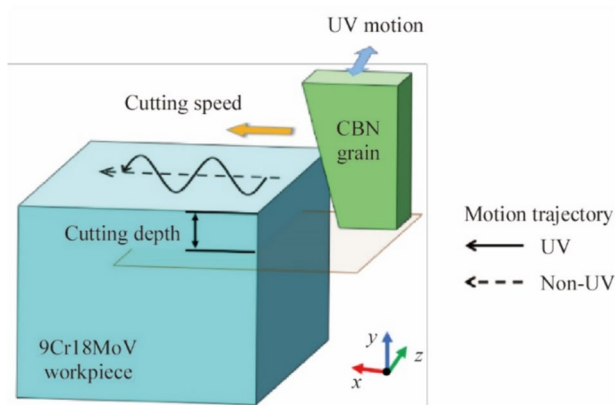
Fig. 3 Single grain scratch test platform

Fig. 4 Relative motion between single-grain and workpiece

Table 1 Parameters of single-grain scratch test

Parameter	Value
Cutting speed/(m·min^{-1})	1, 2, 3, 4
Cutting depth/μm	1, 2, 3, 4
UV condition	Yes / No
UV frequency/Hz	18 000
UV amplitude/μm	4

Table 2 Materials properties [30]

Parameter	Value	
	CBN	9Cr18MoV
Density/(g·cm^{-3})	3.48	7.7
Young's modulus/GPa	710	218
Poisson's ratio	0.12	0.28
Conductivity/(W·(m·K)$^{-1}$)	80	20
Specific heat/(J·(kg·K)$^{-1}$)	430	203
Tensile strength/MPa	700	590
Compressive strength/MPa	2 500	–

Table 3 Parameters of J-C plasticity model

Parameter	Value
A/MPa	350
B/MPa	1 450
C	0.017
n	0.55
m	1.1
T_{melt}/K	1 420
T_{tran}/K	293

The relative motion between the grain and the workpiece is shown in Fig. 4. The main cutting motion of the grain is along the *x*-axis. The cutting depth is altered along the *y*-axis. The UV motion is applied along the *z*-axis.

To correct the installation error of the workpiece and achieve accurate tool feed, the test cutting plane is calibrated by the ruby probe to make it perpendicular to the *y*-axis before cutting. The feeding reference position is confirmed by moving the grain along the *y*-axis until the dynamometer detects the force signal. After the experiment, the morphology and size of burrs were measured by a 3D video microscope (KH-77003Dviewer) and a 3D laser confocal profilometer (S-Neox, SENSOFAR). The test parameters are listed in Table 1.

2.3 Finite element simulation model setup

The properties of CBN grain and 9Cr18MoV are listed in Table 2. The simulation parameters are the same as the test parameters. The cutting depth of single-grain is less than 5 μm during the honing process. To save computing resources, the cutting layer mesh is locally refined, and its mesh size is set to 0.1 μm. The hardness of the CBN grain is far higher than that of the 9Cr18MoV workpiece, so the grain is set to an analytically rigid body.

The material constitutive relation for the workpiece was simulated by the Johnson and Cook constitutive model [31], which has the form of

$$\sigma = \left(A + B\varepsilon_p^n \right) \left(1 + C \left(\ln \frac{\dot{\varepsilon}_p}{\dot{\varepsilon}_0} \right) \right) \left(1 - \left(\frac{T - T_{tran}}{T_{melt} - T_{tran}} \right)^m \right), \tag{2}$$

where B, C, m, n are material constants; ε_p represents the equivalent plastic strain; $\dot{\varepsilon}_p$ and $\dot{\varepsilon}_0$ are the equivalent plastic strain rate and reference strain rate respectively; T_{melt} and T_{tran} are melting temperature and transition temperature, respectively. The parameters used in this study are listed in Table 3.

For the contact between the CBN grain and workpiece, separation was allowed in the normal direction, and sliding
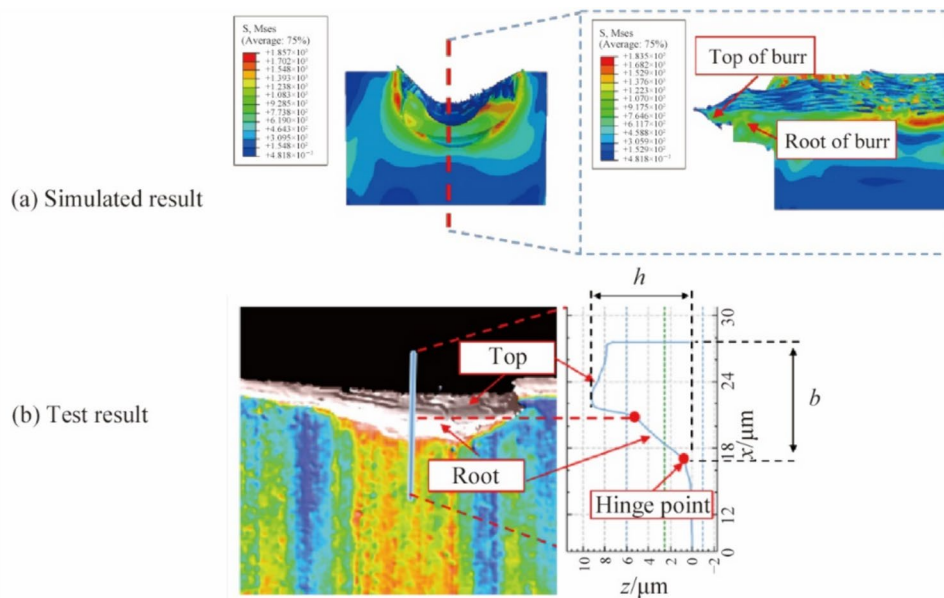
Fig. 5 Burr morphology of simulation and test results

was allowed in the tangential direction, with coulomb frictional resistance. The frictional stress was calculated by

$$\tau = \begin{cases} \mu p \ \left(\text{if } \mu p \leq \tau_{\lim}\right), \\ \tau_{\lim} \ \left(\text{if } \mu p > \tau_{\lim}\right), \end{cases} \tag{3}$$

where p is the normal pressure; friction coefficient μ is set to be 0.3; and $\tau_{\lim}$ is the maximum frictional stress. When the stress becomes larger than $\tau_{\lim}$, the tangential sliding would occur.

The shear damage criterion was applied in this FES model. The damage state variable ω_s was used to numerically describe the material failure process, which increased monotonically with the plastic strain of the elements. It can be calculated as

$$\omega_s = \int_0^{\varepsilon_P} \frac{d\varepsilon_p}{\varepsilon_{s,pl}\left(\theta_s, \dot{\varepsilon}_p\right)} \ \left(0 \leq \omega_s \leq 1\right), \tag{4}$$

where $\varepsilon_{s,pl}\left(\theta_s, \dot{\varepsilon}_p\right)$ is a variable determined by shear ratio θ_s and strain rate $\dot{\varepsilon}_p$. When ω_s reaches 1, the corresponding elements start to fail due to the large plastic strain. In the post-processing, the material state is used to display the final state of each element, which is

$$\text{State value} = \begin{cases} 1 \ \left(\text{if } \omega_s < 1\right), \\ 0 \ \left(\text{if } \omega_s = 1\right). \end{cases} \tag{5}$$

3 Results and analysis

3.1 Indicators of the burr size

Figure 5a shows the simulated burr under 2 m/min of the cutting speed and 3 μm of the cutting depth and non-UV. Figure 5b shows the test result under the same condition measured by the 3D laser confocal profilometer (S-Neox, SENSOFAR). It can be seen from the morphology that the shape of the burr is composed of a top and root. Two indicators are used to evaluate the burr size, which is burr height h and burr thickness b [7]. In simulation, h is 9.4 μm and b is 8.8 μm. In test h is 8.6 μm and b is 10 μm. The discrepancy between the test and simulation results for burr size is less than 15%, which shows good reliability of the simulation.

3.2 Results of the single-grain scratch tests

3.2.1 Influence of various cutting depths on burr size

The test conditions are 2 m/min of cutting speed and 1−5 μm of cutting depth, under UV and non-UV. Figure 6 shows the burr morphology of the test results, and Fig. 7 shows the burr size correspondingly. In both cases, with the increase of the cutting depth, the burr size increased first and then decreased. Under non-UV, the burr size grows with the cutting depth. When the cutting depth is 1 μm, the burr thickness is 5.98
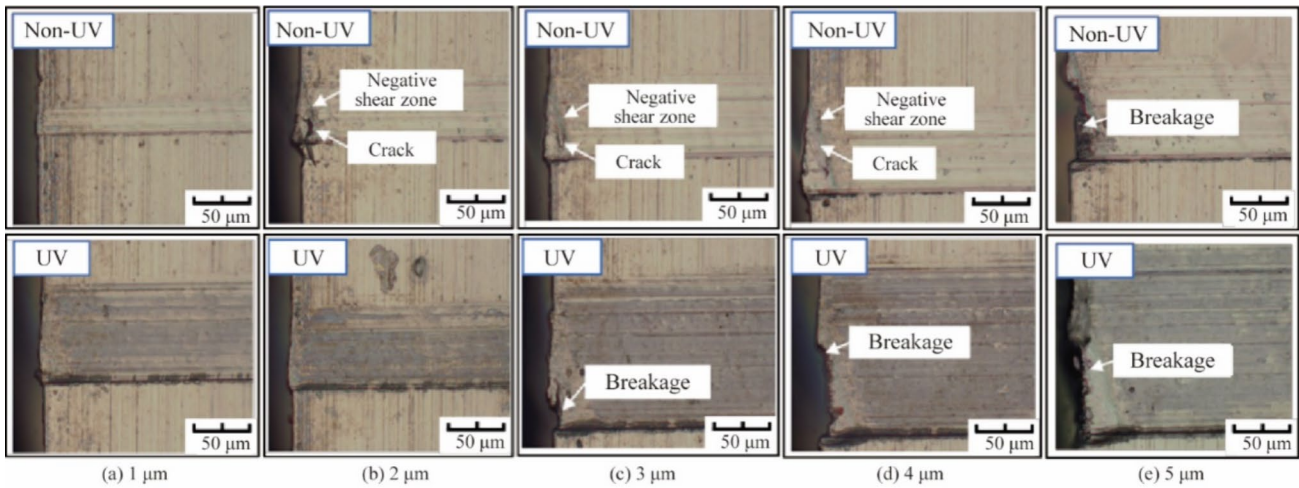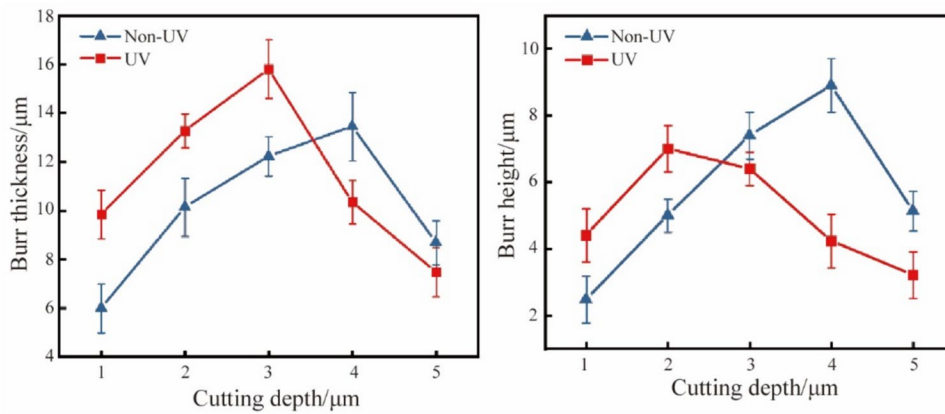
Fig. 6 Test burr morphology at various cutting depths

Fig. 7 Test burr size at various cutting depths

μm, and the burr height is 2.47 μm. When the cutting depth grows to 4 μm, the burr size reaches its maximum which is 13.45 μm in thickness and 8.9 μm in height. When the cutting depth reaches 5 μm, the breakage of the burr happens and the burr size reduces greatly. The burr size drops to 8.68 μm in thickness and 5.13 μm in height.

The trend of burr size under UV is similar to that under non-UV, which is growing initially and then reducing. However, there is a significant difference when the cutting depth is 3 μm. Under UV, the burr partially fractures, leading to an increase in the burr's thickness from 13.27 μm to 15.8 μm and a decrease in its height from 7 μm to 6.4 μm. When the cutting depth is 4 μm, the burr is completely fractured, causing a significant reduction of the burr height. As the cutting depth increases to 5 μm, the breakage is further enlarged, and the burr size drops to 7.47 μm in thickness
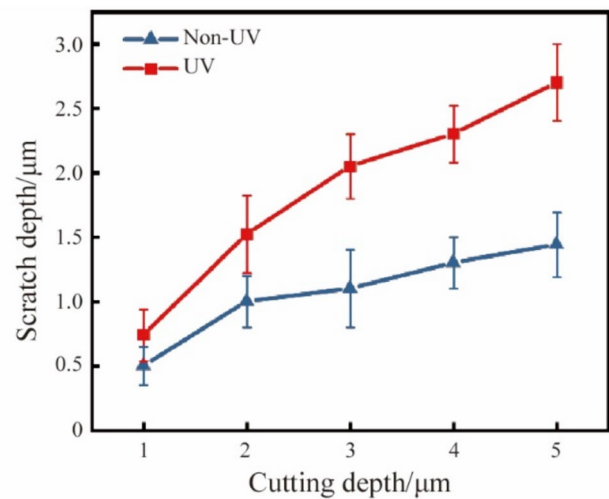

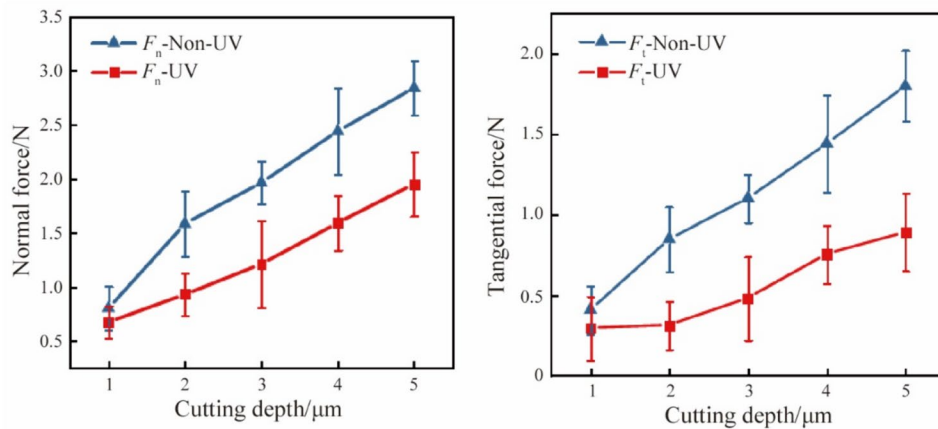**Fig. 8** Scratch depths at various cutting depths

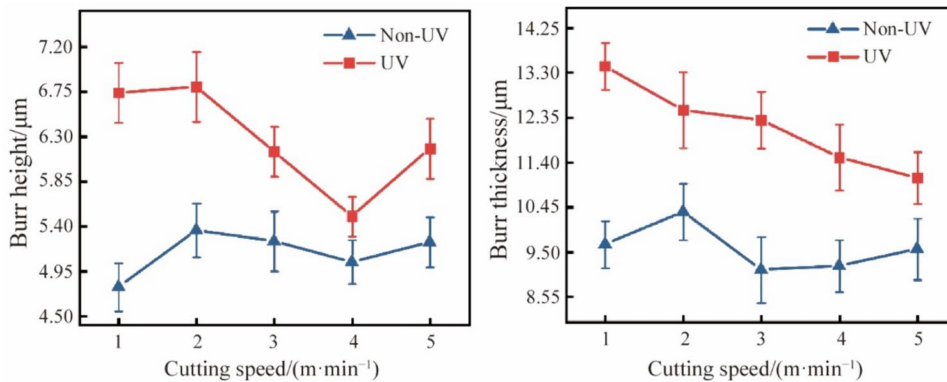**Fig. 9** Cutting forces at various cutting depths

Fig. 10 Burr sizes at various cutting speeds

and 3.21 μm in height. Overall, under UV, the burr size is bigger before the breakage, and smaller after the breakage.

Figure 8 shows the scratch depths of the test results and Fig. 9 shows the cutting forces of the test results. Where F_n is the normal force and F_t is the tangential force. In both situations, the scratch depth and cutting force increase with the cutting depth, but the scratch depths are less than the predetermined cutting depth. Compared to under non-UV, under UV the scratch depth is deeper, and the cutting force is smaller.

3.2.2 Influence of various cutting speeds on burr size

The test conditions are 1−5 m/min of cutting speed and 2 μm of cutting depth, under UV and non-UV. Figure 10 shows the burr sizes at various cutting speeds. The different cutting speed under non-UV has little effect on the burr size, while under UV, the increment of the cutting speed reduces the burr size.
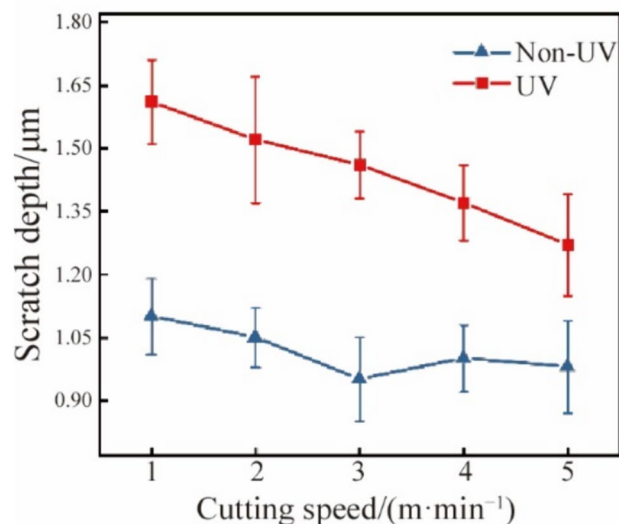

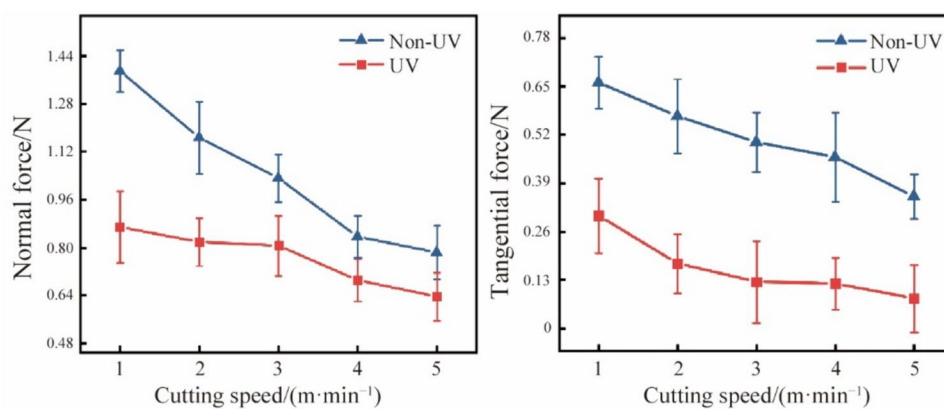**Fig. 11** Scratch depths at various cutting speeds

Fig. 12 Cutting forces at various cutting speeds

(a) Transition stage

(b) Bending deformation stage

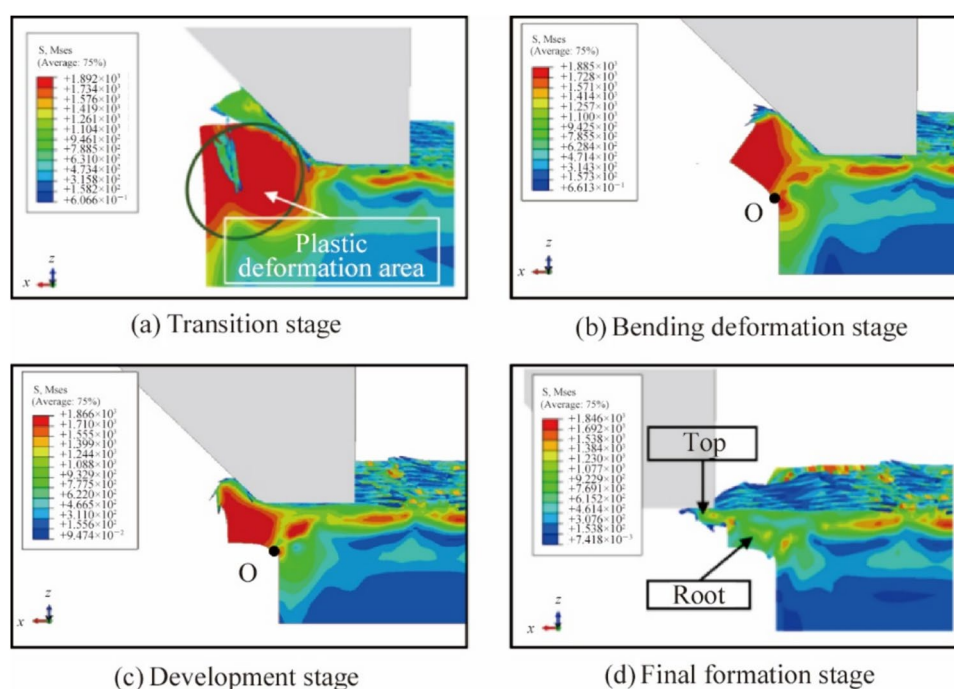(c) Development stage

(d) Final formation stage

Fig. 13 Generation process of burrs

Figure 11 shows the scratch depths at various cutting speeds and Fig. 12 shows the cutting forces at various cutting speeds. In both situations, the scratch depth and the cutting force show a reduction when the cutting speed grows. The scratch depth under UV is deeper than under non-UV, meanwhile, the cutting force is smaller.

4 Mechanism analysis of UV inhibition of burr generation

4.1 Burr's generation stages under non-UV

According to the simulation result, the formation of burrs under non-UV mainly goes through 4 stages. The first stage is the transition stage, as shown in Fig. 13a. As the abrasive grain approaches the edge of the workpiece, the rake face material accumulates, causing the stress to concentrate on the edge of the workpiece gradually. The stiffness of this area reduces as the material decreases. Under the action of
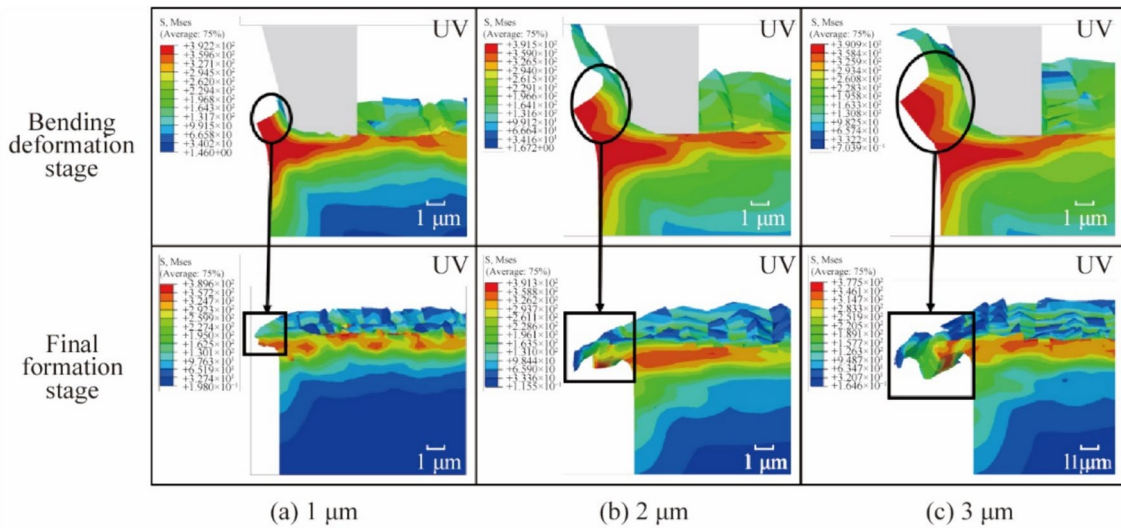
Fig. 14 Relationship between the rake face material volume and burr size

the negative rake angle of the grain, the rake face material gradually produces a tendency of plastic deformation.

The second stage is the bending deformation stage, as shown in Fig. 13b. As the abrasive grain moves further forward, the degree of plastic deformation intensifies. The material at the edge of the workpiece bends around a rotation hinge point O. The actual cutting depth keeps decreasing as the material bends. The cutting action of abrasive grains keeps weakening. More rake face material bends into burrs and less forms chips.

The third stage is the burr development stage, as shown in Fig. 13c. The burr's root is nearly formed when the major

of the material finishes its bending deformation. Most of the rake face material is currently situated beneath the cutting layer, so there are almost no chips forming during this period. As the grain keeps moving forward, the rake face material bends and extends, gradually turning into the burr's top.

The last stage is the final formation stage, as shown in Fig. 13d. When the grain completely cuts out of the workpiece, the burr is completely formed.
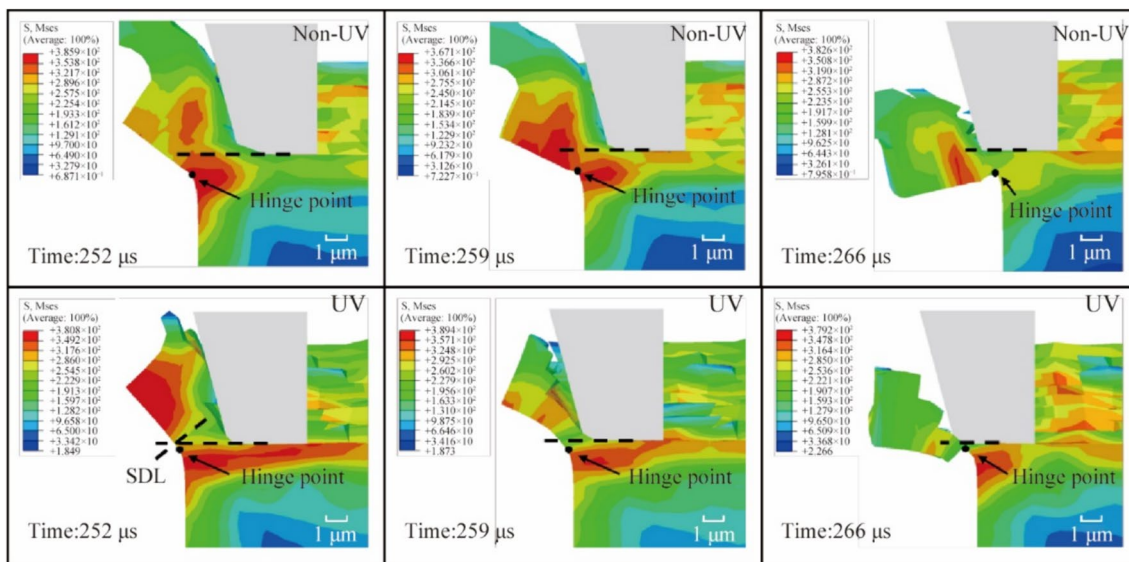

Fig. 15 Stress diagram of the bending deformation stage at 4 μm of cutting depth
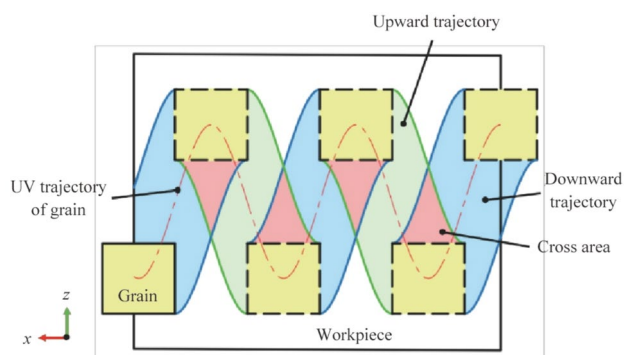
Fig. 16 Schematic diagram of ultrasonic vibration weakening rebound effect

4.2 Analysis of the UV effect on burrs

According to the formation stages of burrs, the burr size mainly depends on the volume of the material on the rake face of the abrasive grain at the bending deformation stage. When the cutting depth grows, the rake face material volume increases and more material rotates around the hinge point, turning into burrs, as shown in Fig. 14. Thus, in both situations, the burr size first grows with the cutting depth.

When the cutting depth is 3 μm, the breakage of the burr is incomplete, making part of the burr extend outward and causing the burr height to increase. But the breakage of the root causes the burr thickness to decrease. When the cutting depth increases to 4 μm, the burr fractures under UV, but not under non-UV. Since the burr fractures at the rotating hinge point, the bending deformation stage of burr formation is crucial in determining whether it breaks. Figure 15 shows the stress diagram of the bending deformation stage at 4 μm of cutting depth. The hinge point under UV is higher than under non-UV, closer to the bottom of the grain which will thin the burr's root

during the development stage. Meanwhile, the higher the hinge point, the more complete the burr fracture, and the smaller the residual burr. Besides, an apparent stress dividing line (SDL) appears near the hinge point. Under the UV effect, the abrasive grain continuously impacts the rake face material and promotes the separation of the stress field. The uneven stress distribution is more susceptible to fatigue fracture in the subsequent bending deformation and reduces the burr size.

In the actual honing process, due to the great amount of the abrasive grains contacting with the workpiece at the same time, the actual cutting depth and normal force of a single grain are usually small which would cause a significant rebound effect. When the grain moves away, the elastic deformation of the material will be released, causing the actual scratch depth to be less than the predetermined cutting depth. While under the effect of UV, the moving direction of the grain is constantly changing, as shown in Fig. 16. The motion trajectory of the grain can be divided into an upward trajectory and a downward trajectory. There are many cross areas between these two, and the rebound material in these areas will be cut again, improving the material removal rate. At the UV parameters used in the tests, for the single-grain scratch process, the cross-area accounts for 29.59% of the total scratch area. And in the honing process, the proportion of crossing trajectories is higher because of the overlap between multi-grain trajectories.

Besides, the high-frequency vibration makes the cutting process of abrasive grain change from continuous cutting to high-frequency intermittent cutting, thus weakening the continuous extrusion effect of the abrasive on the material. The material will withstand multiple alternating loads under the impact of the abrasive, and the pores and cracks increase, reducing the fracture strength of the material [28]. As a result, UV can promote the separation of chips and reduce the cutting force [19].
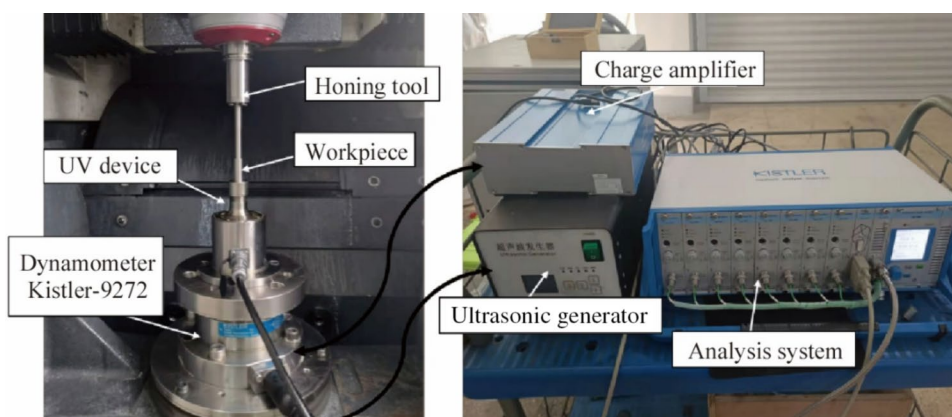

Fig. 17 UAH platform

Table 4 Parameters of honing experiment

Parameter	Value
Honing pressure/MPa	0.2, 0.25, 0.3, 0.35, 0.4
Axial velocity/(m·min⁻¹)	5
Rotate speed/(r·min⁻¹)	1 137
Overtravel distance/mm	6
Reciprocation times/r	200
UV conditions	Yes / No
UV frequency/Hz	18 000
UV amplitude/µm	4

So, the reason for scratch depth under UV being deeper than non-UV can be explained from two aspects. On the one hand, the normal force is much lower, which will weaken the rebound effect. On the other hand, part of the rebound material is removed. As mentioned before, the burr size is mainly dependent on the rake face material volume before the burr fractures, and the material volume is mainly dependent on the actual scratch depth. Since that, when the cutting depth does not exceed 3 µm, the burr size under UV is larger than that under non-UV. In that case, the cutting speed under UV may affect the size of the burr. Due to the fixed frequency and amplitude of UV, the faster the cutting speed, the less the number of vibrations at the edge of the workpiece, which will weaken the UV effect. Besides, the increment of the cutting speed will also lower the cutting force, which weakens the rebound effect. As a result, under the joint action of these two aspects, the scratch depth is decreased as well as the burr size.

5 Verification of the UV effect on burrs in UAH

5.1 UAH test platform set up

To verify the effect of UV on burrs in the honing process, a UAH platform was established to carry out experiments, as shown in Fig. 17. The platform was also built at the DMG ultrasonic 20 Linear ultrasonic assisted machining center. The workpiece is clamped by a UV device, which connects to an ultrasonic generator. The generator can provide a fixed frequency and amplitude of ultrasonic vibration. Dynamometer Kistler-9272 was used to collect the cutting force during the experiment.

The workpiece material is 9Cr18MoV with the hardness of HRC58~64 after heat treatment. The bore of the workpiece was pre-processed to remove the burrs generated by the previous process. The honing tool used is a force-controlled single-stone structure, and the diameter of the abrasive grains fixed on the honing stone is between 165 µm and 198 µm. The parameters used in the honing test are listed in Table 4. When the tests are done, the workpieces are cut along the axis to measure the burr size and morphology by a 3D video microscope (KH-77003Dviewer) and a 3D laser confocal profilometer (S-Neox, SENSOFAR).

5.2 Measurement and evaluation method of honing burr

The honing object is a bore, and the honing burrs are present throughout the circumference. The average burr size at four positions on the circumference is taken as the honing burr size. The measured positions are shown in Fig. 18.

During the honing process, the final honing burrs are formed by all effective grains cutting the edge multiple
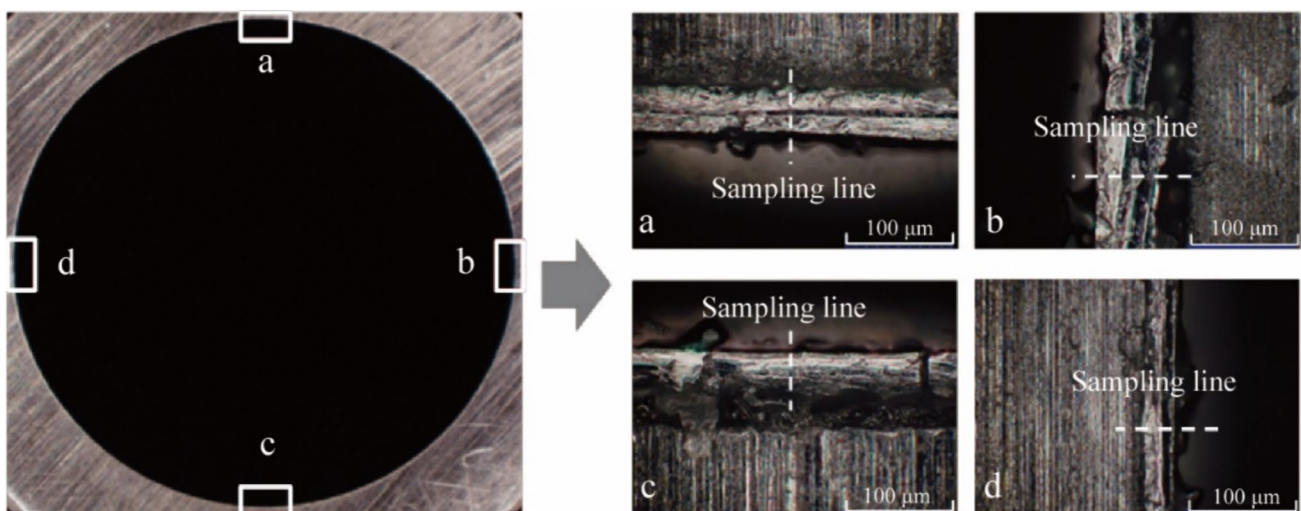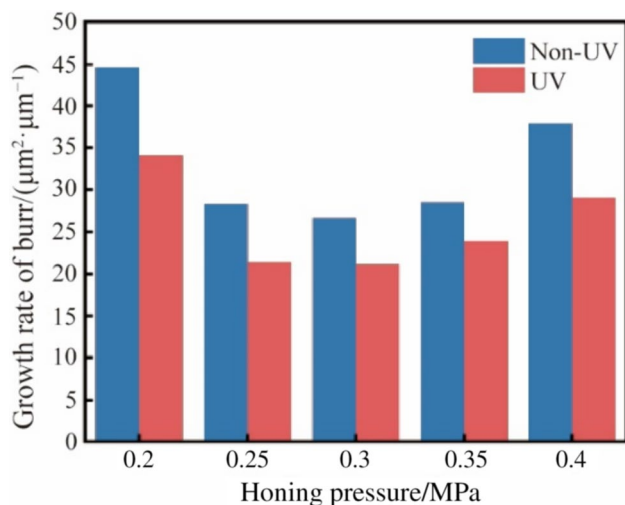

Fig. 18 Honing burr measurement method

Table 5 Measurement results of honing tests

P/MPa	Non-UV			UV		
	b/ μm	h/ μm	Δr/ μm	b/ μm	h/ μm	Δr/ μm
0.2	18	5.45	1.1	22	8.75	2.83
0.25	22	8.3	3.23	23.5	12.75	7
0.3	24	13.43	6.05	27.75	15.13	9.95
0.35	28	14.35	7.05	33	18.5	12.83
0.4	36	15.53	7.38	43.25	22.25	16.58

Fig. 19 Growth rate of burr at various honing pressure

times. Combined with the previous analysis, the growth of the burr is a process that accumulates with material removal. Therefore, to evaluate the honing burrs, the material removal volume needs to be considered. The aperture increment is used to represent the material removal, and it can be measured by a pneumatic aperture measuring instrument.

The growth rate of the burr b_r is defined as the ratio of the cross-sectional area of the burr to the incremental radius Δr of the bore. As the cross-sectional shape of the burr is usually triangular, the growth rate of the burr can be calculated as follows

$$b_r = \frac{bh}{2\Delta r}. \tag{6}$$

5.3 Analysis of the UV effect on burrs in UAH process

The burr sizes and radius increment of honing test results at various honing pressure are shown in Table 5. And the growth rate of the burr is shown in Fig. 19. It can be seen from the results that, in all cases, the radius increment under UV is bigger than under non-UV, and the growth rate of the burr under UV is smaller than under non-UV. The results

prove that UV not only improves the material removal rate greatly but also inhibits the growth of the burr.

6 Conclusions

In this paper, based on the honing condition, the experimental scheme of cutting 9Cr18MoV with a single CBN abrasive grain is designed. How burr's morphology and size change with the cutting parameters under UV and non-UV is studied. Besides, the corresponding simulation model is established. By analyzing the simulation results, the formation mechanism of burrs, the influence mechanism of cutting depth and cutting speed on burr size, and the suppression mechanism of ultrasonic vibration on burr growth are clarified. The conclusions are as follows.

(i) The burr formation process can be divided into the following four stages: the transition stage, the bending deformation stage, the development stage, and the final formation stage. The plastic bending deformation of the rake face material when the grain approaches the edge of the workpiece is the main reason for burr formation. And the burr size is mainly depended on the rake face material volume during the bending deformation stage.

(ii) When the cutting depth is smaller than 5 μm, the rebound effect is significant, making the actual scratch depth smaller than the predetermined cutting depth. The rebound effect is weakened under UV by reducing the cutting force and re-cutting the rebound material. The re-cutting area accounts for 29.59% of the total scratch area. The increment of cutting speed will reduce the proportion of the re-cutting area. The normal cutting force under UV is 31.4% lower than that under non-UV. And the actual scratch depth under UV is 87.5% deeper than that under non-UV. And that makes the burr size under UV bigger than that under non-UV before the burr fractures, which is 1.97 μm larger for burr height, and 3.51 μm larger for burr thickness on average.

(iii) The hinge point under UV is closer to the grain's bottom than non-UV, which makes the material easier to

break when bending around the hinge point. In addition, the abrasive grains have impact characteristics, which can promote the tendency of dividing the stress field at the root of the burr. The uneven stress distribution will increase the possibility of material fracture, which will reduce the fracture strength of the material, so that in the subsequent bending deformation, the burr is more likely to fatigue fracture along the direction of the stress field interface, and ultimately greatly reduce the size of the burr. Under UV, the burr size after fracturing is 44.95% reduced in height and 18.53% reduced in thickness.

(iv) In general, the growth rate of burr under UV is 21.7% lower than that under non-UV. When the honing pressure grows from 0.1 MPa to 0.3 MPa, the growth rate of burr reduces by 39.19%. When the honing pressure keeps growing from 0.3 MPa to 0.5 MPa, the growth rate of burr increases by 39.97%. So, using a honing pressure of 0.3 MPa and applying UV can significantly inhibit the burr's growth.

References

1. Chen ZC, Ge SH, Jiang YL et al (2023) Refined modeling and experimental verification of a torque motor for an electro-hydraulic servo valve. Chin J Aeronaut 36(6):302–317
2. Huang GQ, Mi JC, Yang C et al (2022) CFD-based physical failure modeling of direct-drive electro-hydraulic servo valve spool and sleeve. Sensors 22(19):7559. https://doi.org/10.3390/s22197559
3. Li JY, Yang TY, Wang YW et al (2013) Study of electro-hydraulic force servo system based on flow press servo valve and neural network intelligent control strategy. Appl Mech Mater 427/429:1167–1170
4. Guo H, Lin P, Pan X et al (2019) Development of an automatic grinding system for servo valve spool throttling edge. URAI 2019:718–722. https://doi.org/10.1109/URAI.2019.8768715
5. Chern GL (2006) Experimental observation and analysis of burr formation mechanisms in face milling of aluminum alloys. Int J Mach Tools Manuf 46(12/13):1517–1525
6. Hashimura M, Hassamontr J, Dornfeld DA (1999) Effect of in-plane exit angle and rake angles on burr height and thickness in face milling operation. J Manuf Sci Eng ASME 121(1):13–19
7. Fu D, Ding WF, Yang SB et al (2017) Formation mechanism and geometry characteristics of exit-direction burrs generated in surface grinding of Ti-6Al-4V titanium alloy. Int J Adv Manuf Technol 89(5/8):2299–2313
8. Régnier T, Fromentin G, Marcon B et al (2018) Fundamental study of exit burr formation mechanisms during orthogonal cutting of AlSi aluminium alloy. J Mater Process Technol 257:112–122
9. Liu M (2021) Microscratch of copper by a Rockwell C diamond indenter under a constant load. Nanotechnol Precis Eng 4(3):033003. https://doi.org/10.1063/10.0005065
10. Liu G, Dang J, Chen Y et al (2019) Numerical and experimental investigation on grinding-induced exit burr formation. Int J Adv Manuf Technol 103(5/8):2331–2346
11. Liu J, Yuan W, Xiong J et al (2013) Influence of chamfer size on the two-side direction burr formed in grinding-hardening machine. Adv Mater Res 645:392–395
12. Yang C, Huang J, Xu J et al (2021) Investigation on formation mechanism of the burrs during abrasive reaming based on the single-particle abrasive micro-cutting behavior. Int J Adv Manuf Technol 113(3/4):907–921
13. Liu J, Wang G, Hou D et al (2008) Formation of two side-direction burr in grinding-hardening machining. Proc SPIE 7130. https://doi.org/10.1117/12.819770
14. Wu X, Li L, He N (2017) Investigation on the burr formation mechanism in micro cutting. Precis Eng 47:191–196
15. Chen MJ, Ni HB, Wang ZJ et al (2012) Research on the modeling of burr formation process in micro-ball end milling operation on Ti-6Al-4V. Int J Adv Manuf Technol 62(9/12):901–912
16. Yadav R, Chakladar ND, Paul S (2022) Micro-milling of Ti-6Al-4 V with controlled burr formation. Int J Mech Sci 231:107582. https://doi.org/10.1016/j.ijmecsci.2022.107582
17. Xu J, Gao S, Yang C (2018) Simulation of burr formation during single-pass honing of 4Cr13 stainless steel. ISSAAT 2018
18. Ogorodov VA (2015) Prevention of burring in diamond honing. Russ Eng Res 35:221–226
19. Xu WX, Zhang LC (2015) Ultrasonic vibration-assisted machining: principle, design and application. Adv Manuf 3(3):173–192
20. Liang XL, Zhang CB, Cheung CF et al (2023) Micro/nano incremental material removal mechanisms in high-frequency ultrasonic vibration-assisted cutting of 316L stainless steel. Int J Mach Tools Manuf 191:104064. https://doi.org/10.1016/j.ijmachtools.2023.104064
21. Zhang YB, Yuan ZH, Fang B et al (2023) Study on the mechanism of burr formation by simulation and experiment in ultrasonic vibration-assisted micromilling. Micromachines 14(3):625. https://doi.org/10.3390/mi14030625
22. Chen W, Zheng L, Teng X et al (2019) Finite element simulation and experimental investigation on cutting mechanism in vibration-assisted micro-milling. Int J Adv Manuf Technol 105(11):4539–4549
23. Xu J, Feng P, Feng F et al (2021) Subsurface damage and burr improvements of aramid fiber reinforced plastics by using longitudinal–torsional ultrasonic vibration milling. J Mater Process Technol 297:117265. https://doi.org/10.1016/j.jmatprotec.2021.117265
24. Zhu XX, Wang WH, Jiang RS et al (2020) Research on ultrasonic-assisted drilling in micro-hole machining of the DD6 superalloy. Adv Manuf 8(3):405–417
25. Chang SSF, Bone GM (2010) Burr height model for vibration assisted drilling of aluminum 6061–T6. Precis Eng 34(3):369–375
26. Zai P, Tong J, Liu Z et al (2021) Analytical model of exit burr height and experimental investigation on ultrasonic-assisted high-speed drilling micro-holes. J Manuf Process 68:807–817
27. Li S, Zhang D, Liu C et al (2020) Exit burr height mechanistic modeling and experimental validation for low-frequency vibration-assisted drilling of aluminum 7075–T6 alloy. J Manuf Process 56:350–361
28. Xiang DH, Zhang ZM, Wu BF et al (2020) Effect of ultrasonic vibration tensile on the mechanical properties of high-volume fraction SiCp/Al composite. Int J Precisi Eng Manuf 21(11):2051–2066
29. Gao SW, Yang CY, Xu JH (2018) Experimental study on torque and burrs during ultrasonic assisted single-pass honing of 4Cr13 stainless steel. ISSAAT 2018

30. D'Evelyn MP, Taniguchi T (1999) Elastic properties of translucent polycrystalline cubic boron nitride as characterized by the dynamic resonance method. Diam Relat Mater 8(8):1522–1526
31. Guo YB, Yen DW (2004) A FEM study on mechanisms of discontinuous chip formation in hard machining. J Mater Process Technol 155/156:1350–1356

Peng Wang is currently a master's candidate in Mechanical Engineering at Nanjing University of Aeronautics and Astronautics, People's Republic of China. His research interest is hole machining technology of high efficiency and precision.

Chang-Yong Yang is currently an Associate Professor in Mechanical Engineering at Nanjing University of Aeronautics and Astronautics, People's Republic of China. His research interests include honing and grinding technology of difficult-to-cut materials, super hard abrasive tools and machining process simulation.

Ying-Ying Yuan is currently a Ph.D. candidate in Mechanical Engineering at Nanjing University of Aeronautics and Astronautics, People's Republic of China. Her research interest is hole machining technology of high efficiency and precision.


Yu-Can Fu is currently a Professor in Mechanical Engineering and Doctoral Supervisor at Nanjing University of Aeronautics and Astronautics, People's Republic of China. His research interests include high efficiency machining technology, super abrasive tool technology and green cooling technology.

Wen-Feng Ding is currently a Professor in Mechanical Engineering and Doctoral Supervisor at Nanjing University of Aeronautics and Astronautics, People's Republic of China. His research interests include grinding technology and equipment, super hard abrasive tools, machining process simulation and control technology.

Jiu-Hua Xu is currently a Professor in Mechanical Engineering and Doctoral Supervisor at Nanjing University of Aeronautics and Astronautics, People's Republic of China. His research interests include grinding technology and equipment, super hard abrasive tools, machining process simulation and control technology.
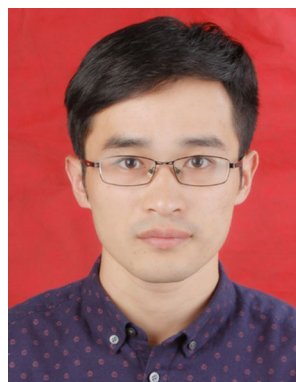
Yong Chen is currently the deputy director of the Technical Center of Suzhou Xinneng Precision Machinery Co., LTD. His research interests include honing equipment design and honing process development.